

High entropy oxide catalysts with SO₂ resistance in RWGS reaction

Mengyuan Zhang ^{a,b,1}, Xiaoyan Lu ^{a,1}, Kongliang Luo ^a, Jian Ye ^a, Jia li Dong ^a, Nana Lu ^a, Xiaopeng Wang ^a, Qiang Niu ^c, Pengfei Zhang ^{a,b,*}, Sheng Dai ^d

^a State Key Laboratory of High-efficiency Utilization of Coal and Green Chemical Engineering, College of Chemistry and Chemical Engineering, Ningxia University, Yinchuan 750021, China

^b School of Chemistry and Chemical Engineering, Shanghai Jiao Tong University, Shanghai 200240, China

^c National Enterprise Technology Center, Inner Mongolia Erdos Electric Power and Metallurgy Group Co., Ltd, Ordos, Inner Mongolia 016064, China

^d Chemical Science Division, Oak Ridge National Laboratory, Oak Ridge TN37830, United States



ARTICLE INFO

Keywords:

High entropy oxide
SO₂ resistance
Entropy engineering
In situ FTIR
In situ XPS
RWGS reaction

ABSTRACT

Ubiquitous presence of SO₂ usually shows adverse effects on industrial catalysis. Herein, a concept of engineering entropy to design SO₂ resistance oxide catalysts is proposed. (Ni_{0.2}Mg_{0.2}Cu_{0.2}Zn_{0.2}Co_{0.2})Fe₂O₄ showed excellent performance (the CO₂ conv. = 41.4%, CO selec. = 99.6% at 400°C) compared to the control samples in the reverse water–gas shift (RWGS). In addition, (Ni_{0.2}Mg_{0.2}Cu_{0.2}Zn_{0.2}Co_{0.2})Fe₂O₄ had the SO₂-tolerant ability (the CO₂ conv. = 38.5%, CO selec. = 99.2% at 400°C) after being poisoned with 1000 ppm SO₂ at 400°C for 1 h. In sharp contrast, the control samples NiFe₂O₄, MgFe₂O₄, CuFe₂O₄ and CoFe₂O₄ lost their activity. O^{1S} XPS indicated that (Ni_{0.2}Mg_{0.2}Cu_{0.2}Zn_{0.2}Co_{0.2})Fe₂O₄ had higher oxygen vacancy concentrations. SO₂ resistance mechanism was studied by infrared spectroscopy, SO₂-TPD, in situ S 2p XPS and the DFT results, confirming that the low SO₂ adsorption energy of (Ni_{0.2}Mg_{0.2}Cu_{0.2}Zn_{0.2}Co_{0.2})Fe₂O₄, which was attributed to the lower Gibbs free energy. This work may inspire the rational design of SO₂-resistant catalysts.

1. Introduction

Heterogeneous catalysis is important for both basic and industrial chemistry. The catalytic performance of solid catalysts is highly correlated with reaction environment. As one of the most important factors, environmental SO₂ inevitably affects industrial catalysis, especially in the real world. SO₂ typically forms sulfites or sulfates on the surface of metal oxide catalysts, causing them to lose activity [1–3]. For example, the presence of SO₂ has a negative impact on the selectivity of products and catalyst activity in the reverse water–gas shift reaction (RWGS). SO₂ would neutralize the active sites on the catalyst surface, leading to a decrease in reaction activity. In industrial applications, SO₂ is usually present in exhaust gas, so the sulfur resistance performance of catalysts is directly related to the stability and economy of RWGS reaction equipment [4,5]. By researching and developing anti SO₂ catalysts, the efficiency of RWGS reaction can be improved, the development of clean energy and carbon capture technology can be promoted. Therefore, catalysts with SO₂ resistance in RWGS reactions is significant. So far,

there are two main ways to design catalysts with SO₂-resistance, including increasing acidity to reduce SO₂ adsorption, and constructing sacrificial sites to protect active sites from SO₂ adsorption. For example, for selective catalytic reduction (SCR) reactions, due to the interaction between sulfate species and iron sites, the acid strength in FeTiO_x catalysts increased, resulting in SO₂ resistance [6]. The Fe element in Fe₈Ce_{1 - δ}VO₄ can effectively inhibit the adsorption of SO₂, making it have good SO₂ resistance in NO_x SCR [7]. For another example, the Fe₂O₃ modified CeO₂ -WO₃ catalyst exhibited high SO₂ resistance in NO_x reduction, due to SO₂ reacted with the Fe₂O₃ outer layer, preventing SO₂ deposition at the active components [3]. Ma et al. reported a MnO_x/CeO₂ nanorod catalyst with SO₂ resistance. Under the condition of 523 K and in the presence of 200 ppm SO₂ for 1000 hours, there was almost no loss of catalyst activity. This was achieved by establishing a dynamic equilibrium between sulfate formation and decomposition on the surface of CeO₂ during the reaction process, thereby reducing the deactivation of MnO_x/CeO₂ active sites [1]. However, the current strategies for improving the sulfur resistance performance of solid

* Corresponding author at: State Key Laboratory of High-efficiency Utilization of Coal and Green Chemical Engineering, College of Chemistry and Chemical Engineering, Ningxia University, Yinchuan 750021, China.

E-mail addresses: pfzhang@nxu.edu.cn, chemistrypf@sjtu.edu.cn (P. Zhang).

¹ Mengyuan Zhang and Xiaoyan Lu contributed equally to this work.

catalysts were quite limited.

To design SO₂-resistant catalysts, both reactant adsorption/activation sites and SO₂ stabilization sites were required, while single metal oxides mostly cannot satisfy. Unlike single metal oxides, high entropy metal oxides (HEOs) are potential in SO₂-resistant catalysts [8–14]. For HEOs, high configurational disorder originated from multiple metal ions sharing a single lattice site, enabling HEOs possess three main characteristics [15–17]. First, different combinations of elements make the high entropy structure adjustable. This characteristic endows HEOs with unexpected characteristics that often exceed low entropy structures [14, 18–20]. For example, the compositional flexibility of HEOs enabled fine-tuning of their catalytic activity and selectivity in Oxygen Evolution Reaction [21]. In addition, the synergistic effect of multiple elements in HEOs provides rich adsorption sites for multi-step series reactions or reactions that require multifunctional catalysts [22–24]. Second, the enhanced configuration entropy can make the foreign metal cations in the oxide lattice more stable, which promotes the formation of oxygen defects and distortions [23]. For example, the relationship between local disorder and distortion in high entropy materials were demonstrated by Ceder et al [20]. Moreover, high entropy materials enabled ions with large ionic radius differences to be jointly dissolved, which led to percolating transport networks with much higher ionic conductivity than those with a single-metal cation component. Third, the sluggish kinetics and high entropy-stabilized structure of HEOs ensured good stabilities for the metal species under reaction conditions [25,26]. HEOs generated a stable single-phase crystal structure by increasing the configuration entropy (Sconfig) of the system. In an equiatomic 5-cation system, the maximum Sconfig value was 1.61 R. Considering the relationship of mixed free energy (ΔG_{mix}) and enthalpy of mixing (ΔH_{mix}), as presented in Equation

$$\Delta G_{mix} = \Delta H_{mix} - T\Delta S_{mix} \quad (1)$$

Therefore, the maximum ΔS_{mix} in HEOs resulted in a low ΔG_{mix} and stable structure. For example, the stability of high entropy (FeNi-CoCrMnV)Ox nanoparticles in oxygen evolution reaction (OER) was two orders of magnitude higher than that of IrO₂ [21]. For another example, high entropy oxide catalyst manufactured by Hu et al. exhibited excellent stability in catalytic methane combustion reactions over 100 hours [26].

Inspired by the high entropy structure and characteristics mentioned above, (Ni_{0.2}Mg_{0.2}Cu_{0.2}Zn_{0.2}Co_{0.2})Fe₂O₄ and control samples AFe₂O₄(A=Ni, Mg, Cu, Zn, Co) were prepared by a ball milling method in this work. The catalytic performance experiment demonstrated that (Ni_{0.2}Mg_{0.2}Cu_{0.2}Zn_{0.2}Co_{0.2})Fe₂O₄ catalysts exhibited extraordinary activity and stability in the reverse water-gas shift (RWGS) reaction compared to the control samples AFe₂O₄(A=Ni, Mg, Cu, Zn, Co). The excellent performance (the CO₂ conv. = 41.4%, CO selec. = 99.6% at 400°C) of (Ni_{0.2}Mg_{0.2}Cu_{0.2}Zn_{0.2}Co_{0.2})Fe₂O₄ showed great advantages of high entropy structures. Furthermore, (Ni_{0.2}Mg_{0.2}Cu_{0.2}Zn_{0.2}Co_{0.2})Fe₂O₄ had the SO₂-tolerant ability (the CO₂ conv. = 38.5%, CO selec. = 99.2% at 400°C) after being poisoned with 1000 ppm SO₂ for 1 h. In sharp contrast, the control sample NiFe₂O₄, MgFe₂O₄, CuFe₂O₄, CoFe₂O₄ lost their activity (the CO₂ conv. <1% at 400°C) after being poisoned. Compared with AFe₂O₄(A=Ni, Mg, Cu, Zn, Co), the SO₂ adsorption ability of (Ni_{0.2}Mg_{0.2}Cu_{0.2}Zn_{0.2}Co_{0.2})Fe₂O₄ was weaker by SO₂-TPD. In situ infrared spectroscopy showed (Ni_{0.2}Mg_{0.2}Cu_{0.2}Zn_{0.2}Co_{0.2})Fe₂O₄ contained less sulfate and sulfite after SO₂ poisoning. In situ XPS results showed that sulfites were more easily reduced to sulfites on (Ni_{0.2}Mg_{0.2}Cu_{0.2}Zn_{0.2}Co_{0.2})Fe₂O₄. DFT calculations and SO₂-TPD indicated that (Ni_{0.2}Mg_{0.2}Cu_{0.2}Zn_{0.2}Co_{0.2})Fe₂O₄ had lower SO₂ adsorption energy compared to single metal AFe₂O₄(A=Ni, Mg, Cu, Zn, Co). In situ FTIR and in situ XPS both matched with the DFT results, explaining the sulfur resistance mechanism. Therefore, a concept of engineering entropy to design SO₂ resistance catalysts was proposed.

2. Experiment

2.1. DFT calculation method

The calculations for the realistic materials were based on the framework of density functional theory (DFT) [27] using the Vienna ab-initio Simulation Package (VASP) [28,29]. The projector augmented wave method was employed to treat core-valence interactions [30,31]. For all calculations, the energy and force convergence criteria were set to be 10⁻⁵ eV and 10⁻³ eV/A under the framework of spin-polarization, respectively. The plane-wave expansion was truncated with a cutoff energy of 520 eV. A vacuum layer of 12 Å is added perpendicular to avoid the interactions between periodic images. The Brillouin zone was sampled with allowed spacing between k points in 0.2 Å⁻¹, with Γ-centered Monkhorst-Pack k-point grid. All the structures are relaxed until the residual forces on the atoms have declined to less than 0.01 eV/Å. The 3D charge density plot is employed by VESTA software [32].

To explore the SO₂ absorption ability of high-entropy oxide surface, the high-entropy oxide surface was constructed by metallic atom random occupation. The absorption energy is defined by:

$$E_{ads} = E[\text{total}] - E[\text{surf}] - E[\text{SO}_2]$$

Where $E[\text{total}]$ is the total energy of the structures after the SO₂ absorption, $E[\text{surf}]$ is the total energy of the surface, that is, high-entropy oxide surface and $E[\text{SO}_2]$ is the energy of one SO₂ molecule.

2.2. Materials

Cu(OAc)₂ (> 99.9%, Aladdin), Zn(OAc)₂ (> 99.9%, Aladdin), Ni(OAc)₂•4H₂O (> 99.9%, Aladdin), Co(OAc)₂•4H₂O (> 99.9%, Aladdin), Mg(OAc)₂•4H₂O (> 99%, Adamas) and Fe(OAc)₃.

2.3. Sample synthesis

(Ni_{0.2}Mg_{0.2}Cu_{0.2}Zn_{0.2}Co_{0.2})Fe₂O₄: 1 mmol Cu(OAc)₂, 1 mmol Zn(OAc)₂, 1 mmol Ni(OAc)₂•4H₂O, 1 mmol Co(OAc)₂•4H₂O, 1 mmol Mg(OAc)₂•4H₂O, and 10 mmol Fe(OAc)₃ were added together to a stainless steel reactor (80 mL) along with 10 stainless steel balls (4×diameter 1.2 cm; 6×diameter 0.5 cm). The reactor was then put on a vibrating ball miller (MSK-SFM-3), and ground for 1 h. Finally, the intermediate was calcined at 400°C for 2 h in air. The ball milling procedure see Fig. 1 in detail. The obtained samples were referred to as (Ni_{0.2}Mg_{0.2}Cu_{0.2}Zn_{0.2}Co_{0.2})Fe₂O₄. The synthesis of the comparison sample was like the above steps, please refer to the supporting materials for details.

2.4. Sample characterization

The X-ray diffraction (XRD) were conducted by PAN analytical X'Pert Pro MPD diffractometer using an X'Celerator RTMS detector. N₂ adsorption-desorption isotherms and specific surface areas were determined by using a TriStar II 3020 volumetric adsorption analyzer. Scanning electron microscopy (Hitachi SU8010) were used to characterize the morphology. High angle annular dark field scanning transmission electron microscopy (HAADF STEM) images were obtained using the Nion Ultra STEM 100 with probe aberration correction. Before testing, choose a regular copper mesh to disperse the powder. In addition, to avoid the interference of Cu from the copper grids, the mapping signals were collected far away from the border of the copper grids. X-ray photoelectron spectroscopy (XPS) testing using monochromatic Al K using AXIS Ultra DLD instruments α X-ray source. 284.6 eV of contaminated carbon C1s serves as a reference for calibrating BE values. The TP-5079 instrument is used for H₂-TPR. Preconditioning 40–60 mesh powder samples (0.05 µg) at 350 °C (5% O₂/He, 30 mL min⁻¹) for 1 h. Reduce to room temperature and increase the temperature to 800 °C

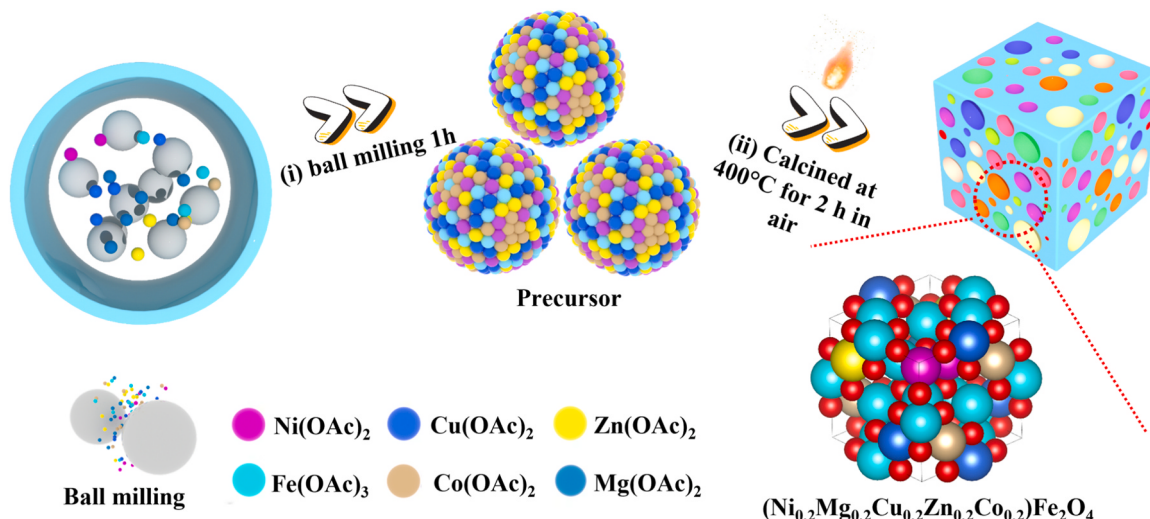


Fig. 1. The synthetic route of high entropy (Ni_{0.2}Mg_{0.2}Cu_{0.2}Zn_{0.2}Co_{0.2})Fe₂O₄. (i) Mixing metal acetates by ball milling. (ii) Calcination of mixed precursors in air.

(5% H₂/He, 30 mL min⁻¹) at a rate of 10 °C min⁻¹, and record using a TCD detector. Static water contact angle (θ W) Using the VCA optimal surface analysis/angle measurement system, the water droplet size is 30 μ L. Perform five measurements on each sample and take the average value. For **SO₂-TPD**, 50–100 mg sample was dried at a temperature programmed from 30°C to 400°C. He airflow (30–50 mL min⁻¹) was purged for 1 hour, cooled to 50°C, and SO₂/N₂ mixture (30–50 mL min⁻¹) was introduced for 1 hour until saturation. He airflow (30–50 mL min⁻¹) was switched to purge for 1 hour to remove weakly physically adsorbed SO₂ on the surface. Finally, the gas was desorbed (800°C, 10°C min⁻¹) under the atmosphere, and the desorbed gas was detected using TCD. Detect the mass spectrometry signal of SO₂. For **in-situ DRIFTS**, using a Thermo IS50 spectrometer equipped with an MCT detector and a high-temperature reaction sample chamber (Praying Mantis, Harris). Before analysis, the sample was treated for 1 h under N₂ flow at 400 °C. Treat the spectrum at the desired temperature as the relative background, and then cool the sample to room temperature. Introduce the reaction gas mixture (30 mL min⁻¹, SO₂: N₂=2:28) into the reaction pool during the programmed heating process. The catalyst sample was treated by the gas flow with a temperature rise from 20°C to 400°C. The sampling interval was 20°C. For **in-situ XRD**, it was performed using Bruker (Germany) model D8 Advance powder diffractometer, equipped with Anton Paar (Austria) XRK900 reaction temperature chamber. The diffractometer is equipped with a high-resolution V Å NTEC-1 position sensitive detector, supplemented by a radial Soller slit system. Conduct in-situ XRD experiments after ball milling with acetate for 0.5 hours. During the experiment, the heating rate was 5 °C min⁻¹ and the temperature increased from 50 °C to 450 °C at 10 °–80 °, with a step size of 0.03 ° and a step size of 0.2 s. The time interval is 5 minutes. The characteristics of X-ray tubes are 40 kV and 40 mA, respectively. For **in-situ XPS**, it was performed in a SPECS instrument equipped with a PHOIBOS 150 MCD 9 analyzer, which operates in FAT mode at a passing energy of 20 eV. Using non monochromate Al K α Radiation (1486.6 eV) excites the electron emission of the sample, and the X-ray source operates at 210 W and 14 kV. Add three to five scans to obtain a separate spectrum. The pressure during the measurement process is maintained within the range of 10–9 millibars. The (Ni_{0.2}Mg_{0.2}Cu_{0.2}Zn_{0.2}Co_{0.2})Fe₂O₄ samples were reduced at 5%H₂/95%N₂ (30 mL min⁻¹) at 500°C for 1 h and cooled to room temperature.

2.5. Catalytic performance test

Firstly, an appropriate amount of quartz cotton (used to support the catalyst) is loaded into a 10 mm diameter glass tube. Then, 50 mg of

catalyst and 100 mg of quartz sand are mixed evenly before being loaded into the reaction tube. Finally, an appropriate amount of quartz cotton is filled. Install the above reaction tube vertically onto the heating furnace and monitor it in real-time using the full name of a thermocouple. First, poison the catalyst in an SO₂ (SO₂:N₂ = 2:28) atmosphere at 400°C for 40 minutes, and then reduce it at 500°C in a 5% H₂/N₂ mixture for 1 hour (10°C min⁻¹, 30 mL min⁻¹) before lowering it to room temperature (< 50°C). Next, switch the feed gas (CO₂: H₂: N₂ = 24%: 72%: 4%, 10°C min⁻¹, 20 mL min⁻¹, GHSV=24000 mL·g⁻¹·h⁻¹) and heat it up to 400°C for reaction for 24 hours. Finally, the GC2060 online gas chromatograph was used with a TDX-01 column as the chromatographic column, H₂ as the carrier gas, and a TCD detector as the detector.

The performance of the catalyst was evaluated using the following indicators:

Carbon dioxide conversion rate:

$$\text{CO}_2 \text{ conversion} = \left[1 - \frac{[\text{N}_2]_{\text{in}} * [\text{CO}_2]_{\text{out}}}{[\text{CO}_2]_{\text{in}} * [\text{N}_2]_{\text{out}}} \right] * 100\% \quad (2)$$

Carbon monoxide selectivity:

$$\text{CO selectivity} = [\text{CO}]_{\text{out}} / ([\text{CO}]_{\text{out}} + [\text{CH}_4]_{\text{out}}) \quad (3)$$

where $[\text{CO}_2]_{\text{in}}$ and $[\text{N}_2]_{\text{in}}$ represent the concentration of CO₂ and N₂ in the inlet, and $[\text{CO}_2]_{\text{out}}$, $[\text{CO}]_{\text{out}}$ and $[\text{CH}_4]_{\text{out}}$ represent the concentrations of each product gas generated in the outlet.

2.6. Calculation of equilibrium conversion rate

The equilibrium conversion rate of RWGS reaction at target temperature in this work is calculated using HSC Chemistry software.

3. Results

3.1. Material preparation and structural characterization

Coprecipitation, solvothermal method and sol gel method are commonly used to construct high entropy metal oxides (HEOs). However, the high temperature for phase transformation (e.g., 900°C–1000 °C) in entropy-driving generally leads to pore collapse and low surface area of the material, thereby inhibiting the catalytic performance of HEOs [11,17,24,33–35]. In this work, (Ni_{0.2}Mg_{0.2}Cu_{0.2}Zn_{0.2}Co_{0.2})Fe₂O₄ and control samples AFe₂O₄(A=Ni, Mg, Cu, Zn, Co) were constructed by a ball milling method. The essence of ball

milling method was the mechanochemical processing of metal precursors, which generated more grain boundaries and interfaces between various metal salts. The description of the procedure was shown in Fig. 1 and Table S1. The accurate content of high entropy oxides were obtained through Inductance-coupled plasma (ICP) analysis (ICP-AES), which were close to the theoretical contents (Table S9).

Initially, in order to explore the crystallization of $(\text{Ni}_{0.2}\text{Mg}_{0.2}\text{Cu}_{0.2}\text{Zn}_{0.2}\text{Co}_{0.2})\text{Fe}_2\text{O}_4$, the calcination process was studied by in situ XRD (Fig. 2a). Amorphous phases were observed between 100°C and 250°C due to the decomposition of metal salts. The diffraction intensity increased and the slope disappeared at 300°C. The characteristic diffusion peaks of cubic phase NiFe_2O_4 (JCPDS 86–2267) appeared and no other diffusion peaks were detected at 400°C. Therefore, the optimal calcination temperature to produce $(\text{Ni}_{0.2}\text{Mg}_{0.2}\text{Cu}_{0.2}\text{Zn}_{0.2}\text{Co}_{0.2})\text{Fe}_2\text{O}_4$ should be 400°C based on in-situ XRD results. Then, the crystal structure of $(\text{Ni}_{0.2}\text{Mg}_{0.2}\text{Cu}_{0.2}\text{Zn}_{0.2}\text{Co}_{0.2})\text{Fe}_2\text{O}_4$ and control samples AFe_2O_4 ($\text{A}=\text{Ni, Mg, Cu, Zn, Co}$) were examined by XRD (Fig. 2b). $(\text{Ni}_{0.2}\text{Mg}_{0.2}\text{Cu}_{0.2}\text{Zn}_{0.2}\text{Co}_{0.2})\text{Fe}_2\text{O}_4$, NiFe_2O_4 , and CoFe_2O_4 all showed characteristic diffraction peaks of cubic phase spinel (JCPDS 86–2267), and no other diffraction peaks were observed. However, pure ZnFe_2O_4 , MgFe_2O_4 , and CuFe_2O_4 spinel could not be obtained under the same preparation conditions of 400°C calcination in air. This result can be understandable considering that the effect of configurational entropy. The Boltzmann equation ($S = K \ln(\omega)$) shows the configuration entropy (ΔS_{config}) increasing with the increase of atomic arrangement number [11,17–19, 36–38]. The ΔS_{config} of transition metal oxide systems can be calculated by the equation: [16,23,25,39–41]

$$\Delta S_{\text{config}} = -R * \left(\sum_{i=1}^n x_i \ln x_i \right)_M \quad (4)$$

where M refers to the cationic element, R is the gas constant, x_i represents the mole fractions of the metal cations, and n is the total number of cation species. By calculation, ΔS_{config} value of $(\text{Ni}_{0.2}\text{Mg}_{0.2}\text{Cu}_{0.2}\text{Zn}_{0.2}\text{Co}_{0.2})\text{Fe}_2\text{O}_4$ is -9.752 , while ΔS_{config} value of single metal AFe_2O_4 ($\text{A}=\text{Ni, Mg, Cu, Zn, Co}$) is -5.287 . This difference would contribute to lower Gibbs free energy ($\Delta G = \Delta H - T\Delta S$) of $(\text{Ni}_{0.2}\text{Mg}_{0.2}\text{Cu}_{0.2}\text{Zn}_{0.2}\text{Co}_{0.2})\text{Fe}_2\text{O}_4$ for crystallization at 400°C. In addition, other typical high entropy metal oxides were also prepared at 400°C, showing characteristic diffraction peaks of cubic phase spinel (JCPDS 86–2267), and no other diffraction peaks were observed (Fig. S1).

In addition, the SEM images showed that $(\text{Ni}_{0.2}\text{Mg}_{0.2}\text{Cu}_{0.2}\text{Zn}_{0.2}\text{Co}_{0.2})\text{Fe}_2\text{O}_4$ was made of aggregated nanoparticles with sizes of 10–30 nm (Fig. 3). Ball milling promoted the formation of small nanoparticles. Furthermore, the TEM images (Fig. 4) further revealed $(\text{Ni}_{0.2}\text{Mg}_{0.2}\text{Cu}_{0.2}\text{Zn}_{0.2}\text{Co}_{0.2})\text{Fe}_2\text{O}_4$ were made of solid nanoparticles. The structure model of $(\text{Ni}_{0.2}\text{Mg}_{0.2}\text{Cu}_{0.2}\text{Zn}_{0.2}\text{Co}_{0.2})\text{Fe}_2\text{O}_4$ was as shown in Fig. 4a. For high-resolution TEM (HRTEM), the lattice spacing was 0.481, 0.251, and 0.295 nm, corresponding to the crystal planes (111), (311), and (220) of the spinel structure (PDF # 86–2267), respectively (Fig. 4b). The scattering area electron diffraction (SAED) results further confirmed the results of HRTEM, which matched well with the typical XRD pattern of NiFe_2O_4 (JCPDS 86–2267) (Fig. 4c). The energy dispersive spectroscopy (EDS) elemental spectrum image showed that Ni, Mg, Cu, Zn, Co, Fe, and O were uniformly distributed within $(\text{Ni}_{0.2}\text{Mg}_{0.2}\text{Cu}_{0.2}\text{Zn}_{0.2}\text{Co}_{0.2})\text{Fe}_2\text{O}_4$, indicating the formation of high entropy oxides (Fig. 4e-1).

Moreover, N_2 sorption measurement at 77 K was carried out (Fig. S10). The specific surface areas of $(\text{Ni}_{0.2}\text{Mg}_{0.2}\text{Cu}_{0.2}\text{Zn}_{0.2}\text{Co}_{0.2})\text{Fe}_2\text{O}_4$ and AFe_2O_4 ($\text{A}=\text{Ni, Mg, Cu, Zn, Co}$) were in the range of 33.9 – $61.4 \text{ m}^2 \text{ g}^{-1}$ (Table S2). The N_2 adsorption curves of $(\text{Ni}_{0.2}\text{Mg}_{0.2}\text{Cu}_{0.2}\text{Zn}_{0.2}\text{Co}_{0.2})\text{Fe}_2\text{O}_4$ and the comparison sample AFe_2O_4 ($\text{A}=\text{Ni, Mg, Cu, Zn, Co}$) both showed the IV type isotherm, indicating that the samples belong to a mesoporous structure and have the potential to facilitate catalytic reactions. The BET specific surface areas of other high entropy oxides (26.0 – $52.8 \text{ m}^2 \text{ g}^{-1}$) were close to that of $(\text{Ni}_{0.2}\text{Mg}_{0.2}\text{Cu}_{0.2}\text{Zn}_{0.2}\text{Co}_{0.2})\text{Fe}_2\text{O}_4$ (Fig. S2). The adsorption curve also showed the characteristics of mesoporous structure.

As is widely known, oxygen vacancies are the most common and studied anionic defects with lower formation energy. In the catalytic reaction process, oxygen vacancies can provide hanging bonds for the adsorption of reaction substrates; Due to its localized electron rich nature, oxygen vacancies can also activate the inert chemical bonds of adsorbed substrates, regulate their electronic structure, and greatly affect the catalytic process [42–44]. Interestingly, the $\text{O}^{1\text{s}}$ XPS results can quantitatively provide oxygen vacancy concentration [45]. Therefore, the surface oxygen species on $(\text{Ni}_{0.2}\text{Mg}_{0.2}\text{Cu}_{0.2}\text{Zn}_{0.2}\text{Co}_{0.2})\text{Fe}_2\text{O}_4$ and control samples AFe_2O_4 ($\text{A}=\text{Ni, Mg, Cu, Zn, Co}$) were characterized by XPS (Fig. 5b–g). Generally, the peak at 529.9 eV represents the lattice oxygen (O^α) and the peak at 531.5 eV represents the oxygen vacancy (O^β). The ratio of $\text{O}^\beta/\text{O}^\alpha$ can reflect the oxygen vacancy concentration [46]. The value of $\text{O}^\beta/\text{O}^\alpha$ of control samples were between 0.81 and 2.27 (Table S3). In sharp contrast, the value of $\text{O}^\beta/\text{O}^\alpha$ in $(\text{Ni}_{0.2}\text{Mg}_{0.2}\text{Cu}_{0.2}\text{Zn}_{0.2}\text{Co}_{0.2})\text{Fe}_2\text{O}_4$ were much higher (up to 3.88), confirming that

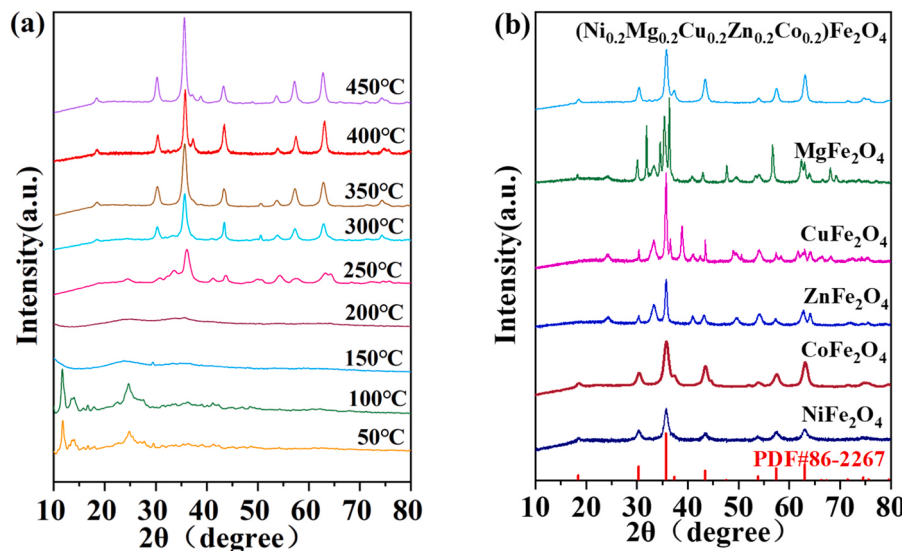


Fig. 2. (a) In situ XRD patterns of $(\text{Ni}_{0.2}\text{Mg}_{0.2}\text{Cu}_{0.2}\text{Zn}_{0.2}\text{Co}_{0.2})\text{Fe}_2\text{O}_4$ Catalysts during the programmed heating temperature. (b) X-ray diffraction patterns of $(\text{Ni}_{0.2}\text{Mg}_{0.2}\text{Cu}_{0.2}\text{Zn}_{0.2}\text{Co}_{0.2})\text{Fe}_2\text{O}_4$ and comparative samples AFe_2O_4 ($\text{A}=\text{Ni, Mg, Cu, Zn, Co}$).

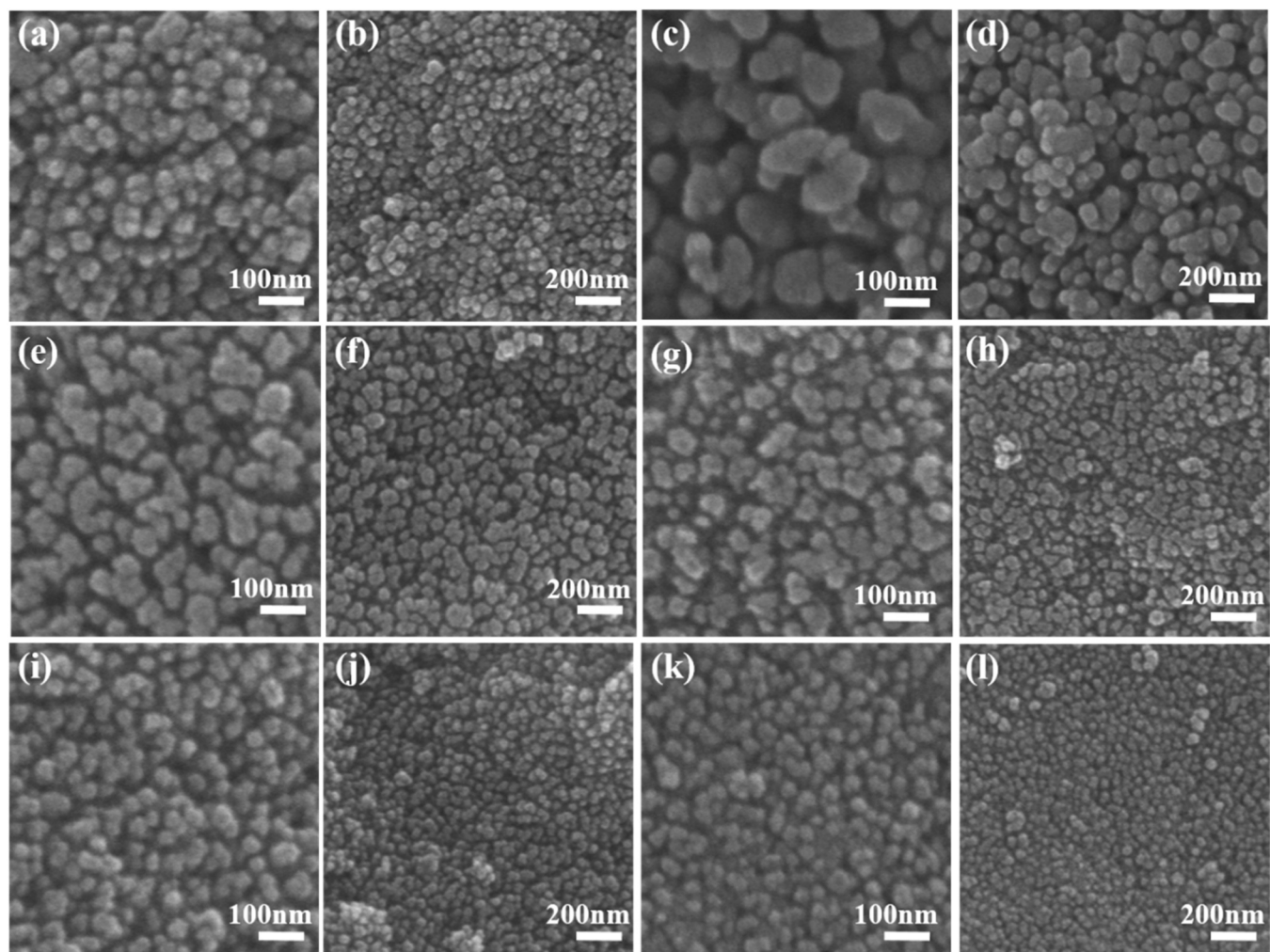


Fig. 3. (a-b) SEM images of $(\text{Ni}_{0.2}\text{Mg}_{0.2}\text{Cu}_{0.2}\text{Zn}_{0.2}\text{Co}_{0.2})\text{Fe}_2\text{O}_4$, (c-d) SEM of NiFe_2O_4 , (e-f) SEM of MgFe_2O_4 , (g-h) SEM of CuFe_2O_4 , (i-j) SEM of ZnFe_2O_4 and (k-l) SEM of CoFe_2O_4 .

the high oxygen vacancies concentration in $(\text{Ni}_{0.2}\text{Mg}_{0.2}\text{Cu}_{0.2}\text{Zn}_{0.2}\text{Co}_{0.2})\text{Fe}_2\text{O}_4$. This is reasonable considering that the high entropy oxides structure (e.g., A-O-B asymmetric metal-oxygen bonds, lattice distortion, and delayed dynamics of oxygen spreading) [8]. The high oxygen vacancy concentration in $(\text{Ni}_{0.2}\text{Mg}_{0.2}\text{Cu}_{0.2}\text{Zn}_{0.2}\text{Co}_{0.2})\text{Fe}_2\text{O}_4$ had the potential to enhance catalytic performance compared to the control samples AFe_2O_4 ($\text{A}=\text{Ni, Mg, Cu, Zn, Co}$).

Then, H_2 -TPR of $(\text{Ni}_{0.2}\text{Mg}_{0.2}\text{Cu}_{0.2}\text{Zn}_{0.2}\text{Co}_{0.2})\text{Fe}_2\text{O}_4$ and comparative samples AFe_2O_4 ($\text{A}=\text{Ni, Mg, Cu, Zn, Co}$) were carried out to further evaluate the redox property of metal species in oxides (Fig. 6a). For NiFe_2O_4 , the peak at 436°C was due to the reduction of NiFe_2O_4 to Ni [47]. Among these comparative samples AFe_2O_4 ($\text{A}=\text{Ni, Mg, Cu, Zn, Co}$), CuFe_2O_4 showed the lowest reduction temperature (281°C), attributing to the reduction of CuFe_2O_4 to Cu . This is reasonable considering that the weak bond of $\text{Cu}-\text{O}$ (42KJ mol^{-1}) [48] would lead to the good oxygen supply capacity of CuO . Interestingly, the reduction peaks of $(\text{Ni}_{0.2}\text{Mg}_{0.2}\text{Cu}_{0.2}\text{Zn}_{0.2}\text{Co}_{0.2})\text{Fe}_2\text{O}_4$ were not similar to those of five single metal oxides. This result revealed that five metals occupy the same oxide lattice in $(\text{Ni}_{0.2}\text{Mg}_{0.2}\text{Cu}_{0.2}\text{Zn}_{0.2}\text{Co}_{0.2})\text{Fe}_2\text{O}_4$, matching well with XRD and TEM results (Fig. 2 and Fig. 4). For $(\text{Ni}_{0.2}\text{Mg}_{0.2}\text{Cu}_{0.2}\text{Zn}_{0.2}\text{Co}_{0.2})\text{Fe}_2\text{O}_4$, the consumption of H_2 at 225°C was due to the removal of surface adsorbed oxygen. While the center position of the first peak of $(\text{Ni}_{0.2}\text{Mg}_{0.2}\text{Cu}_{0.2}\text{Zn}_{0.2}\text{Co}_{0.2})\text{Fe}_2\text{O}_4$ (262°C) was lower than that of CuFe_2O_4 (281°C). This is attributed to the reduction of Cu . Therefore, compared to the comparative sample AFe_2O_4 ($\text{A}=\text{Ni, Mg, Cu, Zn, Co}$),

the corresponding metal ions in $(\text{Ni}_{0.2}\text{Mg}_{0.2}\text{Cu}_{0.2}\text{Zn}_{0.2}\text{Co}_{0.2})\text{Fe}_2\text{O}_4$ appear to be more easily reduced, which is expected to improve catalytic performance.

3.2. The catalytic performance experiment

The Reverse Water Gas Shift (RWGS) reaction utilizes renewable H_2 to directly hydrogenate CO_2 into CO , providing a suitable method for producing various value-added chemicals through Fischer Tropsch synthesis or other synthesis gas processes [4,49–52]. Due to the significant ability to activate CO_2 and economic feasibility, iron based catalysts have been widely developed. However, the main challenge is that SO_2 (typically 1–10 ppm) in the exhaust gas causes severe deactivation of iron-based catalysts, which leads to a low RWGS efficiency [7,53]. Therefore, it is exceedingly desirable to develop iron-based catalysts with superior SO_2 resistance. The $(\text{Ni}_{0.2}\text{Mg}_{0.2}\text{Cu}_{0.2}\text{Zn}_{0.2}\text{Co}_{0.2})\text{Fe}_2\text{O}_4$ and comparative samples AFe_2O_4 ($\text{A}=\text{Ni, Mg, Cu, Zn, Co}$) were applied to RWGS. As shown in Figs. 5a, S5 and S6, the CO_2 conversion rate of $(\text{Ni}_{0.2}\text{Mg}_{0.2}\text{Cu}_{0.2}\text{Zn}_{0.2}\text{Co}_{0.2})\text{Fe}_2\text{O}_4$ was 41.4% in the reverse water-gas shift (RWGS) at 400°C , which was higher than that of the comparison samples NiFe_2O_4 (36.1%), MgFe_2O_4 (33.6%), CuFe_2O_4 (38.1%), ZnFe_2O_4 (35.3%) and CoFe_2O_4 (34.9%). In addition, the CO selectivity of $(\text{Ni}_{0.2}\text{Mg}_{0.2}\text{Cu}_{0.2}\text{Zn}_{0.2}\text{Co}_{0.2})\text{Fe}_2\text{O}_4$ was 99.6%, which was higher than the comparison samples NiFe_2O_4 (96.1%), MgFe_2O_4 (97.5%), CuFe_2O_4 (97.7%), ZnFe_2O_4 (99.2%) and CoFe_2O_4 (94.9%) (Table S5). The results

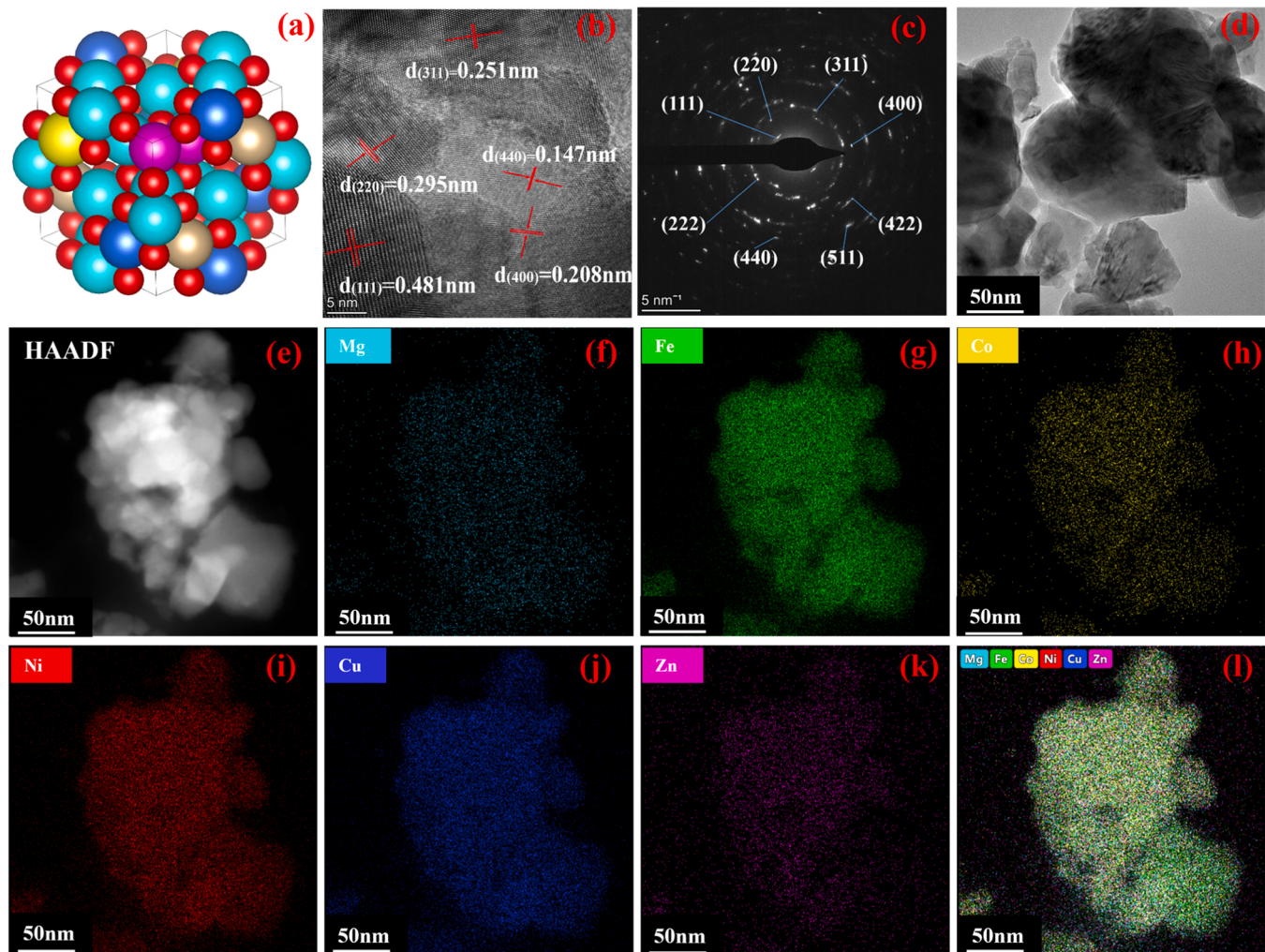


Fig. 4. (a) A structure model of $(\text{Ni}_{0.2}\text{Mg}_{0.2}\text{Cu}_{0.2}\text{Zn}_{0.2}\text{Co}_{0.2})\text{Fe}_2\text{O}_4$ by ball milling. (b) The HRTEM image of $(\text{Ni}_{0.2}\text{Mg}_{0.2}\text{Cu}_{0.2}\text{Zn}_{0.2}\text{Co}_{0.2})\text{Fe}_2\text{O}_4$ sample. (c) SAED pattern of $(\text{Ni}_{0.2}\text{Mg}_{0.2}\text{Cu}_{0.2}\text{Zn}_{0.2}\text{Co}_{0.2})\text{Fe}_2\text{O}_4$ sample. (d) The TEM images of $(\text{Ni}_{0.2}\text{Mg}_{0.2}\text{Cu}_{0.2}\text{Zn}_{0.2}\text{Co}_{0.2})\text{Fe}_2\text{O}_4$ sample. (e) HAADFS-STEM image and (f-l) Energy-dispersive spectroscopy (EDS) elemental mapping images of $(\text{Ni}_{0.2}\text{Mg}_{0.2}\text{Cu}_{0.2}\text{Zn}_{0.2}\text{Co}_{0.2})\text{Fe}_2\text{O}_4$ nanoparticles.

of catalytic performance were consistent with that of O^{1s} XPS and H₂-TPR. Other types of high entropy metal oxides also exhibit excellent catalytic performance (Figs. S3–S4 and Table S4). In addition, the performance of commercial Cu-Zn-Al catalysts and the catalysts prepared in this work in RWGS were summarized in Table S8. The $(\text{Ni}_{0.2}\text{Mg}_{0.2}\text{Cu}_{0.2}\text{Zn}_{0.2}\text{Co}_{0.2})\text{Fe}_2\text{O}_4$ catalyst exhibited excellent catalytic performance compared with commercial RWGS catalysts at 400°C.

In addition, to explore the SO₂ resistance performance of catalysts, the catalysts were poisoned by 1000 ppm SO₂ for 1 h at 400°C. Then, the catalysts were reduced in 5% H₂/N₂ for 1 h at 400°C, and the RWGS activity was reevaluated under CO₂/H₂/N₂ (24%: 72%: 4%) atmosphere at 400°C. It can be observed that the NiFe₂O₄, MgFe₂O₄, CuFe₂O₄, and CoFe₂O₄ catalysts displayed poor activity (CO₂ conv. <1%) after 1 h continuous poisoning by 1000 ppm SO₂. Commercial Cu-Zn-Al catalyst also gradually lose activity within 15 hours (Fig. S9). It was very likely that the formation of SO₂²⁻ caused the irreversible activity loss. In contrast, $(\text{Ni}_{0.2}\text{Mg}_{0.2}\text{Cu}_{0.2}\text{Zn}_{0.2}\text{Co}_{0.2})\text{Fe}_2\text{O}_4$ catalyst demonstrated relatively slow activity decay (CO₂ conv. = 38.5%, CO₂ selec. = 99.2%) and exhibited the best SO₂ tolerance and still being stable within 200 hours (Figs. 5b, S7 and S8 and Table S6). This indicated the high entropy structure being potential to improve the SO₂ tolerance. It was understandable considering that the high entropy structure endowed high entropy oxides(HEOs) with two potential features for SO₂ resistance catalysis [54]. First, the lower Gibbs free energy of high entropy oxides

catalysts is expected to make it more stable than single metal oxide, even under SO₂-containing conditions. Second, various metal components with reactant adsorption sites, reactive sites for activation, and SO₂ non-adsorption sites could be combined into single-phase HEOs catalysts. In this regard, tuning entropy in oxides may contribute to SO₂ resistance catalysis.

3.3. The mechanism of SO₂ resistance

O^{1s} XPS results have confirmed that the high oxygen vacancies concentration in $(\text{Ni}_{0.2}\text{Mg}_{0.2}\text{Cu}_{0.2}\text{Zn}_{0.2}\text{Co}_{0.2})\text{Fe}_2\text{O}_4$ compared to that of control samples. The electron transfer process of oxygen vacancies in catalysts is crucial for regulating the interaction between catalysts and SO₂. When oxygen vacancies exist, they tend to provide electrons to metal sites, forming metal oxygen bonds. This electron transfer makes metal sites more electron rich, while oxygen vacancies themselves become electron donors. In the process of SO₂ oxidation, the catalyst needs to extract electrons from SO₂ to promote the oxidation reaction. Since oxygen vacancies have already supplied electrons to metal sites, metal sites are more likely to extract the required electrons from SO₂. The result of this electron transfer is a slowing down of the catalyst's oxidation activity towards SO₂, as the metal sites have already received electron support, thereby reducing their demand for electrons in SO₂. Therefore, oxygen vacancies competitively reduce the electron transfer

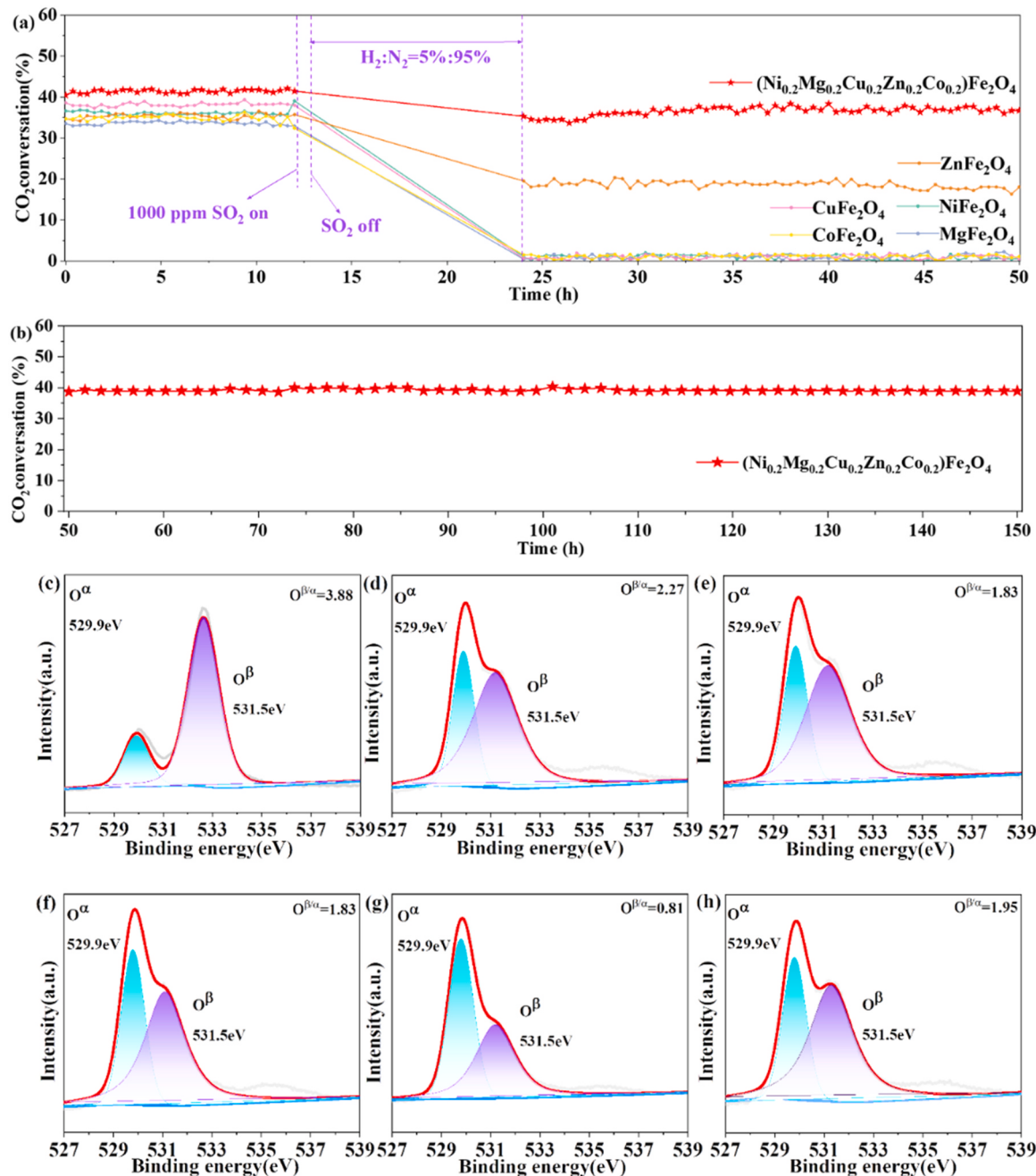


Fig. 5. (a) The catalytic performance of (Ni_{0.2}Mg_{0.2}Cu_{0.2}Zn_{0.2}Co_{0.2})Fe₂O₄ and single metal AFe₂O₄(A=Ni, Mg, Cu, Zn, Co) in RWGS before and after introducing 1000 ppm SO₂ at 400°C. (b) Stability experiment of (Ni_{0.2}Mg_{0.2}Cu_{0.2}Zn_{0.2}Co_{0.2})Fe₂O₄ in RWGS after introducing 1000 ppm SO₂ at 400°C for 100 h. (Reaction conditions: feed gas CO₂/H₂/N₂ molar ratios of 24/72/4, GHSV=24000 mL·g⁻¹·h⁻¹). O^{1s} XPS spectra of (c) (Ni_{0.2}Mg_{0.2}Cu_{0.2}Zn_{0.2}Co_{0.2})Fe₂O₄, (d) CuFe₂O₄, (e) MgFe₂O₄, (f) NiFe₂O₄, (g) ZnFe₂O₄, (h) CoFe₂O₄.

rate between the catalyst and SO₂, achieving inhibition of SO₂ oxidation reaction. Due to the fact that SO₂ oxidation is usually a key step leading to sulfur poisoning, this regulatory mechanism effectively reduces the occurrence of sulfur poisoning. The mechanism of sulfur resistance is that oxygen vacancies limit the oxidation reaction of SO₂ by adjusting the surface electron distribution of the catalyst. This regulatory effect improves the stability of the catalyst in environments containing sulfur substances and extends its service life. Overall, oxygen vacancies regulate the interaction between catalysts and SO₂ at the electronic level by promoting electron transfer, providing an effective regulatory mechanism for sulfur resistance. For example, Wang et al. constructed MnCeSmTiO_x amorphous mixed oxides. Doping Sm in MnCeSmTiO_x can increase oxygen vacancies, which is beneficial for the active adsorption

of NO₂, bidentate nitrate, and bridging nitrate intermediates. It also suppresses SO₂ poisoning by inhibiting the oxidation of SO₂ by Mn⁴⁺ and Ce⁴⁺ [55]. For another example, Hu et al. designed a strong sulfur resistant cerium dioxide based catalyst. The sulfur resistance of catalysts was closely related to the electronic state of cerium dioxide. When the Ce³⁺/Ce⁴⁺ratio increased, cerium dioxide appeared in a non bulk electronic state, where the catalyst exhibited strong sulfur resistance [56].

To further explore the reason why high entropy (Ni_{0.2}Mg_{0.2}Cu_{0.2}Zn_{0.2}Co_{0.2})Fe₂O₄ had stronger SO₂ resistance than that of the control samples AFe₂O₄(A=Ni, Mg, Cu, Zn, Co) (Fig. 5a), the pristine surface chemical states of (Ni_{0.2}Mg_{0.2}Cu_{0.2}Zn_{0.2}Co_{0.2})Fe₂O₄ and the control samples (after 1 h SO₂ poisoning at 400°C) were first investigated by S 2p XPS (Fig. S11). The peak at around 169.5 eV correspond to

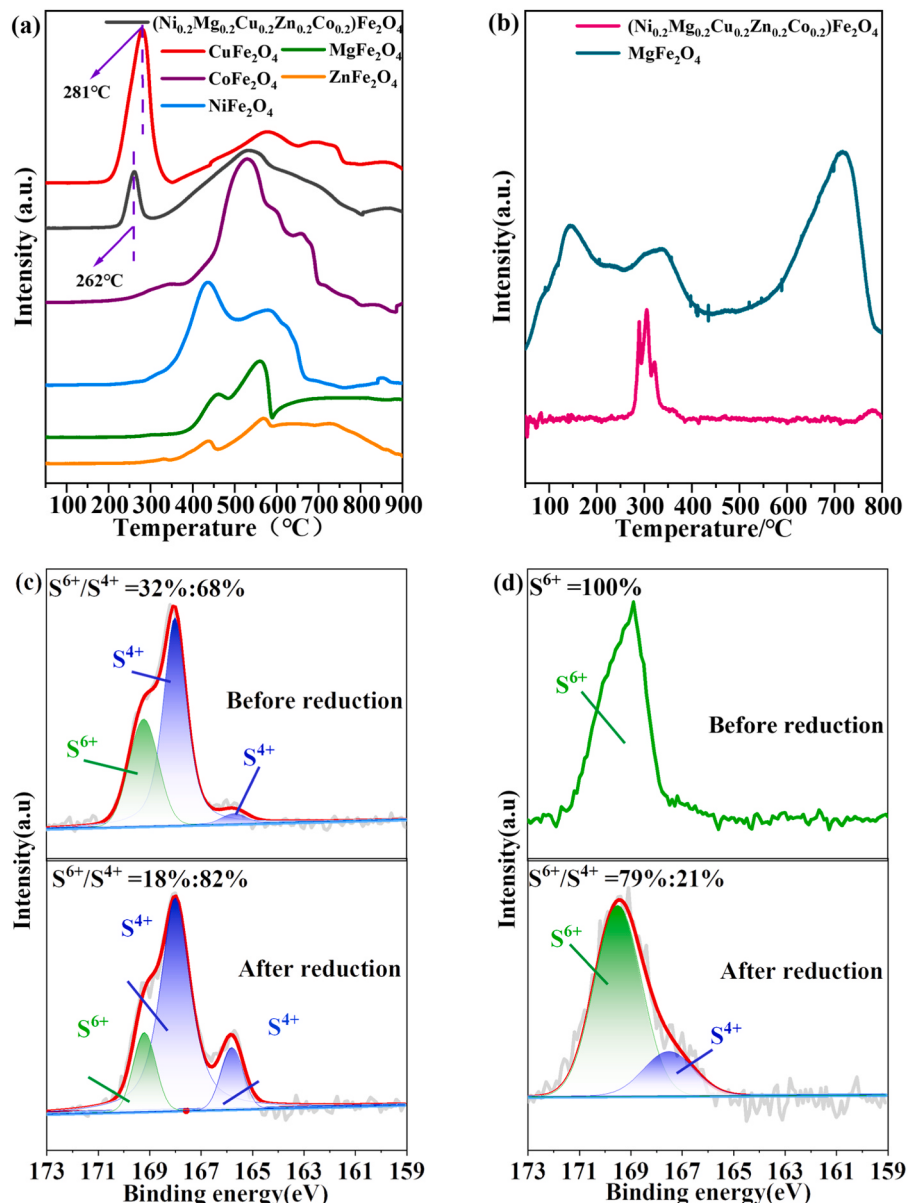


Fig. 6. (a) H₂-TPR profiles of (Ni_{0.2}Mg_{0.2}Cu_{0.2}Zn_{0.2}Co_{0.2})Fe₂O₄ and comparative samples AFe₂O₄(A=Ni, Mg, Cu, Zn, Co). (b) Sulfur dioxide-temperature programmed desorption (SO₂-TPD) profiles of (Ni_{0.2}Mg_{0.2}Cu_{0.2}Zn_{0.2}Co_{0.2})Fe₂O₄ and the comparative sample MgFe₂O₄. (c) S 2p XPS spectra of (Ni_{0.2}Mg_{0.2}Cu_{0.2}Zn_{0.2}Co_{0.2})Fe₂O₄, (d) S 2p XPS spectra of CuFe₂O₄ before reduction and after reduction at 500°C in 5%H₂/95%N₂ (The spectra directly below is after reduction, while the spectra directly above is before reduction).

the S⁶⁺. Two peaks were present around 167.5 and 165.8 eV, corresponding to the S⁴⁺. By integrating the peak area and obtaining the ratio, it is possible to quantitatively reflect the proportion of different sulfur species. The relative ratio of S⁶⁺/S⁴⁺ in (Ni_{0.2}Mg_{0.2}Cu_{0.2}Zn_{0.2}Co_{0.2})Fe₂O₄ was 32%: 68%, indicating that after 1 h 1000 ppm SO₂ poisoning, more sulfites remained on the high entropy sample. In sharp contrast, only S⁶⁺ species were detected in the control samples AFe₂O₄(A=Ni, Mg, Cu, Zn, Co), indicating that all were sulfates. According to reports [57,58], the presence of sulfates would cause severe deactivation of the catalyst and Sulfate was more likely to cause catalyst poisoning and deactivation than sulfite. This result was consistent with the poor SO₂ resistance performance of the control samples AFe₂O₄(A=Ni, Mg, Cu, Zn, Co) in RWGS.

To further study the effect of high entropy structure on SO₂ resistance behavior, in-situ S 2p XPS of (Ni_{0.2}Mg_{0.2}Cu_{0.2}Zn_{0.2}Co_{0.2})Fe₂O₄ and the control sample CuFe₂O₄ were conducted (Fig. 6c, d). For both (Ni_{0.2}Mg_{0.2}Cu_{0.2}Zn_{0.2}Co_{0.2})Fe₂O₄ and the control sample CuFe₂O₄, In-

situ XPS results revealed that high chemical valence state S⁶⁺ has been converted to a low chemical valence state S⁴⁺ partially by 5% H₂/N₂ at 500°C. In high entropy samples (Ni_{0.2}Mg_{0.2}Cu_{0.2}Zn_{0.2}Co_{0.2})Fe₂O₄, some sulfates were reduced to sulfites by 5% H₂/N₂, slowing down the poisoning of sulfur dioxide. The ratio of the S⁶⁺ and S⁴⁺ was 32%: 68% initially and 18%: 82% after reduction in (Ni_{0.2}Mg_{0.2}Cu_{0.2}Zn_{0.2}Co_{0.2})Fe₂O₄. At the same time, a part of S⁶⁺ (21%) ions have been reduced into S⁴⁺ in CuFe₂O₄. However, due to the high sulfate content (S⁶⁺=100%) in the comparison sample CuFe₂O₄, even after H₂ reduction, it still had a high sulfate content (S⁶⁺=79%), resulting in the deactivation of the catalyst in the comparison sample CuFe₂O₄.

Then, SO₂-TPD measurements were performed on (Ni_{0.2}Mg_{0.2}Cu_{0.2}Zn_{0.2}Co_{0.2})Fe₂O₄ and the control sample MgFe₂O₄ to evaluate the absorption capacity of SO₂ and the number of adsorption sites (Fig. 6b). MgFe₂O₄ exhibited significant desorption peaks at low or moderate temperatures (150°C, 350°C, and 700°C). This indicated that MgFe₂O₄ had a strong ability to absorb SO₂. In stark contrast, there was a

desorption peak in the medium to low temperature range (320°C) for $(\text{Ni}_{0.2}\text{Mg}_{0.2}\text{Cu}_{0.2}\text{Zn}_{0.2}\text{Co}_{0.2})\text{Fe}_2\text{O}_4$, indicating weak adsorption of SO_2 or relatively low thermal stability of the adsorbed species on $(\text{Ni}_{0.2}\text{Mg}_{0.2}\text{Cu}_{0.2}\text{Zn}_{0.2}\text{Co}_{0.2})\text{Fe}_2\text{O}_4$. The results of in-situ S 2p XPS and SO_2 -TPD matched well with the results of anti SO_2 catalytic performance (Fig. 5a).

Moreover, the in-situ diffuse reflectance infrared spectroscopy (in-situ IR) can be used for catalyst characterization and reaction mechanism research under working conditions. In Fig. 7, after introducing 1000 ppm SO_2 with balanced N_2 , the in-situ IR was applied to speculate the formation process of sulfates on the $(\text{Ni}_{0.2}\text{Mg}_{0.2}\text{Cu}_{0.2}\text{Zn}_{0.2}\text{Co}_{0.2})\text{Fe}_2\text{O}_4$ and the control samples AFe_2O_4 ($\text{A}=\text{Ni, Mg, Cu, Zn, Co}$). The peak at 1380 cm^{-1} is attributed to SO_2 which being physically adsorbed. The peak of 1125 cm^{-1} is attributed to SO_4^{2-} species, while the peak of 975 cm^{-1} is attributed to SO_3^{2-} species [2,7,57,59,60]. For the high entropy sample $(\text{Ni}_{0.2}\text{Mg}_{0.2}\text{Cu}_{0.2}\text{Zn}_{0.2}\text{Co}_{0.2})\text{Fe}_2\text{O}_4$, the intensity of the two peaks 1125 cm^{-1} and 975 cm^{-1} were very weak and did not change over time with 1000 ppm SO_2 . This indicated that a small amount of SO_2 was

adsorbed on the surface of $(\text{Ni}_{0.2}\text{Mg}_{0.2}\text{Cu}_{0.2}\text{Zn}_{0.2}\text{Co}_{0.2})\text{Fe}_2\text{O}_4$, and a small amount of sulfate and sulfite were generated. In sharp contrast, for the comparison sample, the peak signals of 1125 cm^{-1} and 975 cm^{-1} were very strong, and they became stronger as the temperature increased. The above results suggested that large amounts of physically adsorbed SO_2 , sulfate and sulfite species were deposited on the surface of the control samples AFe_2O_4 ($\text{A}=\text{Ni, Mg, Cu, Zn, Co}$) catalyst, which would cover the active sites and deactivate the catalyst.

To further study the effect of high entropy structure on sulfur resistance and its mechanism, DFT calculations were conducted. A site ($\text{A}=\text{Ni, Mg, Cu, Zn, Co}$) in AFe_2O_4 were tuned from single to five metal ions. The adsorption energy of SO_2 on the surface of single metal AFe_2O_4 ($\text{A}=\text{Ni, Mg, Cu, Zn, Co}$) and $(\text{Ni}_{0.2}\text{Mg}_{0.2}\text{Cu}_{0.2}\text{Zn}_{0.2}\text{Co}_{0.2})\text{Fe}_2\text{O}_4$ were calculated respectively (Fig. 8, Table S7). The adsorption energy of SO_2 on the surfaces of single metal AFe_2O_4 ($\text{A}=\text{Ni, Mg, Cu, Zn, Co}$) were $-1.43\sim-2.28\text{ eV}$ (220) and $-1.75\sim-2.53\text{ eV}$ (311). In contrast, the presence of SO_2 molecules on the surface of $(\text{Ni}_{0.2}\text{Mg}_{0.2}\text{Cu}_{0.2}\text{Zn}_{0.2}\text{Co}_{0.2})\text{Fe}_2\text{O}_4$ had low adsorption energy with -0.57 eV (220) and -0.61 eV

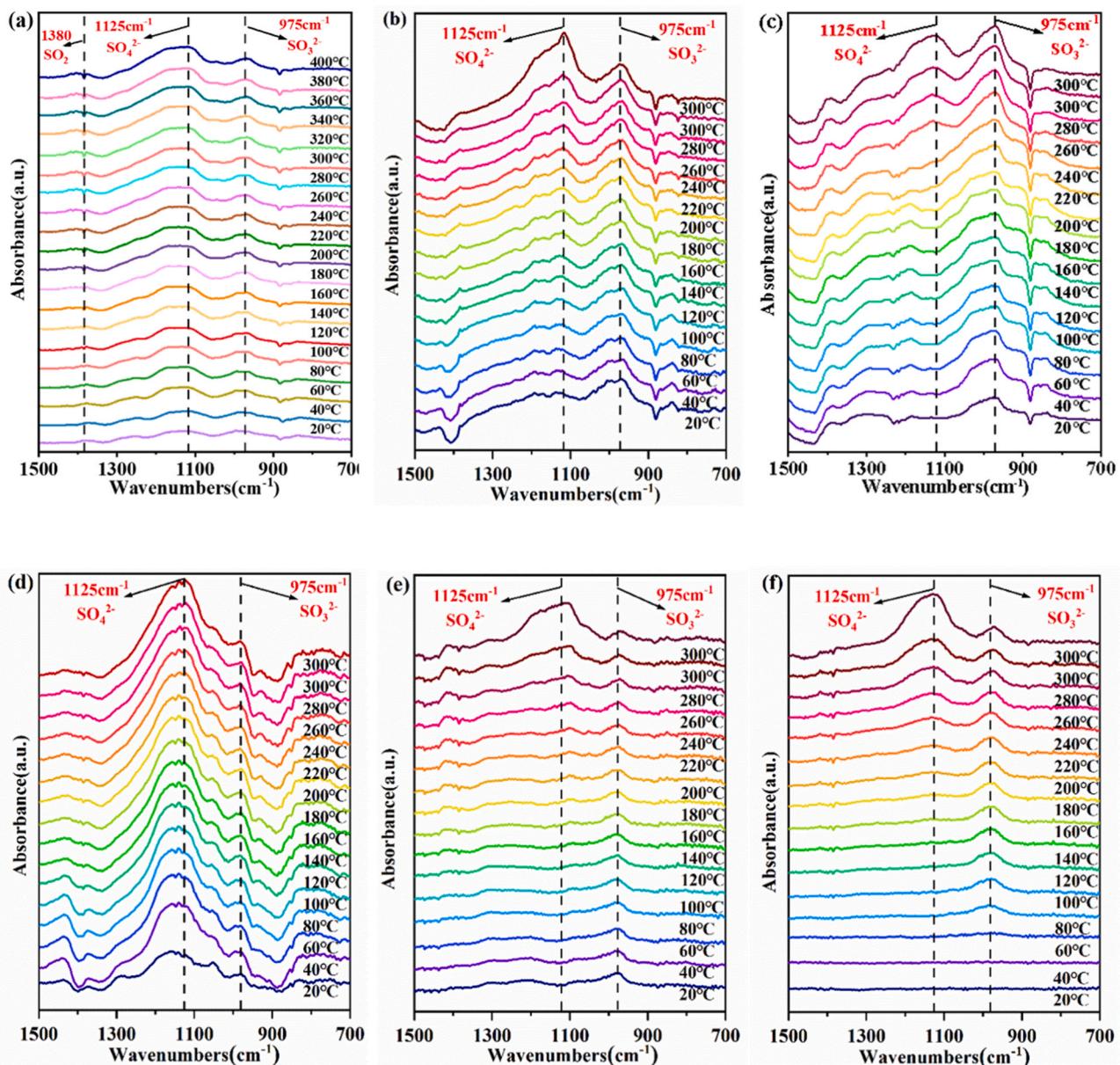


Fig. 7. In situ DRIFT spectra for (a) $(\text{Ni}_{0.2}\text{Mg}_{0.2}\text{Cu}_{0.2}\text{Zn}_{0.2}\text{Co}_{0.2})\text{Fe}_2\text{O}_4$, (b) NiFe_2O_4 , (c) MgFe_2O_4 , (d) CuFe_2O_4 , (e) ZnFe_2O_4 and (f) CoFe_2O_4 catalyst at different temperature with 1000 ppm SO_2 ; sampling interval was 20°C.

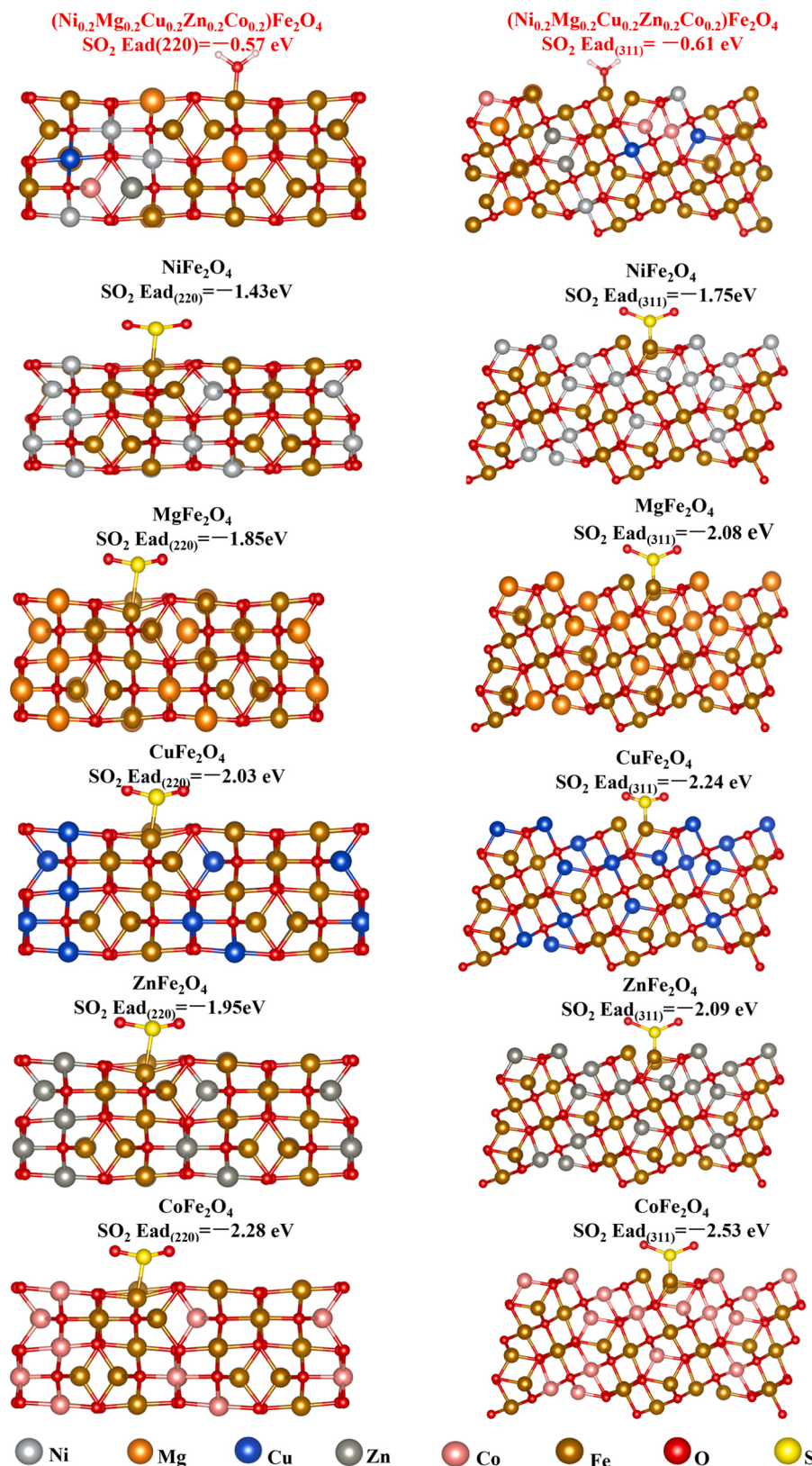


Fig. 8. The adsorption energy of SO₂ on the surface of high entropy (Ni_{0.2}Mg_{0.2}Cu_{0.2}Zn_{0.2}Co_{0.2})Fe₂O₄ and single metal AFe₂O₄(A=Ni, Mg, Cu, Zn, Co) at crystal plane (220) and (311) respectively.

(311). It seems like high-entropy structure could decrease the adsorption of SO₂ compared to single metal AFe₂O₄(A=Ni, Mg, Cu, Zn, Co). The results of in situ infrared spectroscopy and DFT calculation were both consistent with the results of SO₂-resistant catalytic performance, SO₂-TPD and in situ S 2p XPS.

Supplementary Material Additional figures, tables and the discussion are available in **Supplementary Material**.

4. Conclusion

To sum up, inspired by the principle of high entropy-stabilized structure, a concept of engineering entropy to design SO₂ resistance oxide catalysts is proposed. The (Ni_{0.2}Mg_{0.2}Cu_{0.2}Zn_{0.2}Co_{0.2})Fe₂O₄ showed excellent performance (the CO₂ conv. = 41.4%, CO selec. = 99.6% at 400°C) compared to the control sample AFe₂O₄(A=Ni, Mg, Cu, Zn, Co) in the reverse water-gas shift (RWGS). In addition, (Ni_{0.2}Mg_{0.2}Cu_{0.2}Zn_{0.2}Co_{0.2})Fe₂O₄ had the SO₂-tolerant ability (the CO₂ conv. = 38.5%, CO selec. = 99.2% at 400°C) after being poisoned with 1000 ppm SO₂ for 1 h. In sharp contrast, the control sample NiFe₂O₄, MgFe₂O₄, CuFe₂O₄ and CoFe₂O₄ lost the activity(the CO₂ conv. <1% at 400°C). Compared with single metal AFe₂O₄(A=Ni, Mg, Cu, Zn, Co), the SO₂ adsorption ability of (Ni_{0.2}Mg_{0.2}Cu_{0.2}Zn_{0.2}Co_{0.2})Fe₂O₄ was weaker by SO₂-TPD. The mechanism of SO₂ resistance of (Ni_{0.2}Mg_{0.2}Cu_{0.2}Zn_{0.2}Co_{0.2})Fe₂O₄ was further studied through in-situ infrared spectroscopy and In situ XPS, showing that (Ni_{0.2}Mg_{0.2}Cu_{0.2}Zn_{0.2}Co_{0.2})Fe₂O₄ contained less sulfate and sulfite after SO₂ poisoning, compared to single metal AFe₂O₄(A=Ni, Mg, Cu, Zn, Co). SO₂-TPD, in situ FTIR, in situ XPS and the DFT results all confirmed the low SO₂ adsorption energy of (Ni_{0.2}Mg_{0.2}Cu_{0.2}Zn_{0.2}Co_{0.2})Fe₂O₄ compared to single metal AFe₂O₄(A=Ni, Mg, Cu, Zn, Co), which was attributed to the lower Gibbs free energy. High entropy oxides were first successfully prepared in 2015, and multiphase catalysis applications began to emerge around 2018. The application of high entropy oxides in multiphase catalysis is promising and fresh [8]. The design of anti SO₂ catalysts based on engineering entropy will provide inspiration for the design of SO₂-resistant catalysts.

CRediT authorship contribution statement

Zhang Pengfei: Writing – review & editing, Funding acquisition. **Zhang Mengyuan:** Writing – review & editing, Writing – original draft, Methodology, Investigation, Formal analysis. **Lu Xiaoyan:** Validation, Software, Conceptualization. **Luo Kongliang:** Resources, Methodology. **Ye Jian:** Data curation. **Dong Jia li:** Resources. **Lu Nana:** Software. **Wang Xiaopeng:** Investigation. **Niu Qiang:** Validation. **Dai Sheng:** Writing – review & editing.

Declaration of Competing Interest

The authors declare that they have no known competing financial interests or personal relationships that could have appeared to influence the work reported in this paper.

Data availability

Data will be made available on request.

Acknowledgements

This work was supported by the National Key R & D Program Plan (2020YFB0606400), the National Natural Science Foundation of China (Grant Nos. 21776174; 22178219), the Inner Mongolia Key R & D Program Plan (2021ZD0042), the Shanghai Rising-Star Program (20QA1405200), and the Shanghai Jiao Tong University Scientific and Technological Innovation Funds (No. 2019QYB06). S.D. (discussion of the results) was supported by U.S. Department of Energy, Office of

Science, Basic Energy Sciences, Materials Sciences and Engineering Division.

Appendix A. Supporting information

Supplementary data associated with this article can be found in the online version at doi:10.1016/j.apcatb.2024.123845.

References

- [1] Z. Ma, L. Sheng, X. Wang, W. Yuan, S. Chen, W. Xue, G. Han, Z. Zhang, H. Yang, Y. Lu, Y. Wang, *Adv. Mater.* 31 (2019) 1903719.
- [2] N. Sadokhina, G. Smedler, U. Nylen, M. Olofsson, L. Olsson, *Appl. Catal. B Environ.* 236 (2018) 384–395.
- [3] L. Kang, L. Han, J. He, H. Li, T. Yan, G. Chen, J. Zhang, L. Shi, D. Zhang, *Environ. Sci. Technol.* 53 (2019) 938–945.
- [4] E. Pahija, C. Panaritis, S. Gusarov, J. Shadbahr, F. Bensebaa, G. Patience, D. C. Boffito, *ACS Catal.* 12 (2022) 6887–6905.
- [5] X. Fang, Y. Liu, Y. Cheng, W. Cen, *ACS Catal.* 11 (2021) 4125–4135.
- [6] F. Liu, K. Asakura, H. He, W. Shan, X. Shi, C. Zhang, *Appl. Catal. B Environ.* 103 (2011) 369–377.
- [7] L. Kang, L. Han, P. Wang, C. Feng, J. Zhang, T. Yan, J. Deng, L. Shi, D. Zhang, *Environ. Sci. Technol.* 54 (2020) 14066–14075.
- [8] C. Oses, C. Toher, S. Curtarolo, *Nat. Rev. Mater.* 5 (2020) 295–309.
- [9] H. Qi, L. Chen, S. Deng, J. Chen, *Nat. Rev. Mater.* (2023).
- [10] A. Sarkar, Q. Wang, A. Schiele, M.R. Chellali, S.S. Bhattacharya, D. Wang, T. Brezesinski, H. Hahn, L. Velasco, B. Breitung, *Adv. Mater.* 31 (2019) e1806236.
- [11] D. Feng, Y. Dong, L. Zhang, X. Ge, W. Zhang, S. Dai, Z.-A. Qiao, *Angew. Chem. Int. Ed.* 59 (2020) 19503–19509.
- [12] J. Liu, Y. Li, Z. Chen, N. Liu, L. Zheng, W. Shi, X. Wang, *J. Am. Chem. Soc.* 144 (2022) 23191–23197.
- [13] B. Jiang, C.A. Bridges, R.R. Unocic, K.C. Pitike, V.R. Cooper, Y. Zhang, D.-Y. Lin, K. Page, *J. Am. Chem. Soc.* 143 (2021) 4193–4204.
- [14] S.S. Aamlid, M. Oudah, J. Rottler, A.M. Hallas, *J. Am. Chem. Soc.* 145 (2023) 5991–6006.
- [15] L. Fan, Y. Ji, G. Wang, J. Chen, K. Chen, X. Liu, Z. Wen, *J. Am. Chem. Soc.* 144 (2022) 7224–7235.
- [16] Y. Luo, S. Hao, S. Cai, T.J. Slade, Z.Z. Luo, V.P. Dravid, C. Wolverton, Q. Yan, M. G. Kanatzidis, *J. Am. Chem. Soc.* 142 (2020) 15187–15198.
- [17] Y. Sun, S. Dai, *Sci. Adv.* 7 (2021) eabg1600.
- [18] K. Gu, D. Wang, C. Xie, T. Wang, G. Huang, Y. Liu, Y. Zou, L. Tao, S. Wang, *Angew. Chem. Int. Ed.* 60 (2021) 20253–20258.
- [19] A. Sarkar, L. Velasco, D. Wang, Q. Wang, G. Talasila, L. de Biasi, C. Kubel, T. Brezesinski, S.S. Bhattacharya, H. Hahn, B. Breitung, *Nat. Commun.* 9 (2018) 3400.
- [20] Y. Zeng, B. Ouyang, J. Liu, Y.-W. Byeon, Z. Cai, L.J. Miara, Y. Wang, G. Ceder, *Science* 378 (2022) 1320–1324.
- [21] A. Abdelhafiz, B. Wang, A.R. Harutyunyan, J. Li, *Adv. Energy Mater.* 12 (2022) 2200742.
- [22] Y. Yao, Q. Dong, A. Brozena, J. Luo, J. Miao, M. Chi, C. Wang, I.G. Kevrekidis, Z. J. Ren, J. Greeley, G. Wang, A. Anapolsky, L. Hu, *Science* 376 (2022) eabn3103.
- [23] B. Ward-O'Brien, E.J. Pickering, R. Ahumada-Lazo, C. Smith, X.L. Zhong, Y. Aboura, F. Alam, D.J. Binks, T.L. Burnett, D.J. Lewis, *J. Am. Chem. Soc.* 143 (2021) 21560–21566.
- [24] Y. Yao, Z. Huang, P. Xie, S.D. Lacey, R.J. Jacob, H. Xie, F. Chen, A. Nie, T. Pu, M. Rehwoldt, D. Yu, M.R. Zachariah, C. Wang, R. Shahbazian-Yassar, J. Li, L. Hu, *Science* 359 (2018) 1489–1494.
- [25] H. Xu, Z. Zhang, J. Liu, C.-L. Do-Thanh, H. Chen, S. Xu, Q. Lin, Y. Jiao, J. Wang, Y. Wang, Y. Chen, S. Dai, *Nat. Commun.* 11 (2020) 3908.
- [26] T. Li, Y. Yao, Z. Huang, P. Xie, Z. Liu, M. Yang, J. Gao, K. Zeng, A.H. Brozena, G. Pastel, M. Jiao, Q. Dong, J. Dai, S. Li, H. Tong, M. Chi, J. Luo, Y. Mo, G. Wang, C. Wang, R. Shahbazian-Yassar, L. Hu, *Nat. Catal.* 4 (2021) 62–70.
- [27] W. Kohn, L.J. Sham, *Phys. Rev.* 140 (1965) A1133–A1138.
- [28] G. Kresse, J. Furthmüller, *Phys. Rev. B* 54 (1996) 11169–11186.
- [29] G.K. A, J.Fb.J.C.M, *Science* 6 (1996) 15–50.
- [30] G. Kresse, D.J.P.R.B.C.M. Joubert, *Comput. Mater. Sci.* 59 (1999).
- [31] J.P. Perdew, Y.J.Pr.B. Wang, *Condens. Matter Phys. Rev. B* 45 (1992) 13244–13249.
- [32] K. Momma, F.J.Jo.A.C. Izumi, *J. Appl. Crystallogr.* 44 (2011).
- [33] L. Su, H. Huyan, A. Sarkar, W. Gao, X. Yan, C. Addiego, R. Kruk, H. Hahn, X. Pan, *Nat. Commun.* 13 (2022) 2358.
- [34] X. Wang, Q. Dong, H. Qiao, Z. Huang, M.T. Saray, G. Zhong, Z. Lin, M. Cui, A. Brozena, M. Hong, Q. Xia, J. Gao, G. Chen, R. Shahbazian-Yassar, D. Wang, L. Hu, *Adv. Mater.* 32 (2020) 2070341.
- [35] Y. Xin, S. Li, Y. Qian, W. Zhu, H. Yuan, P. Jiang, R. Guo, L. Wang, *ACS Catal.* 10 (2020) 11280–11306.
- [36] R. Witte, A. Sarkar, R. Kruk, B. Eggert, R.A. Brand, H. Wende, H. Hahn, *Phys. Rev. Mater.* 3 (2019) 034406.
- [37] L. Tang, Y. Yang, H. Guo, Y. Wang, M. Wang, Z. Liu, G. Yang, X. Fu, Y. Luo, C. Jiang, Y. Zhao, Z. Shao, Y. Sun, *Adv. Funct. Mater.* 2112157.
- [38] J. Zhang, J. Yan, S. Calder, Q. Zheng, M.A. McGuire, D.L. Abernathy, Y. Ren, S. H. Lapidus, K. Page, H. Zheng, J.W. Freeland, J.D. Budai, R.P. Hermann, *Chem. Mater.* 31 (2019) 3705–3711.

[39] J. Zhao, J. Bao, S. Yang, Q. Niu, R. Xie, Q. Zhang, M. Chen, P. Zhang, S. Dai, *ACS Catal.* 11 (2021) 12247–12257.

[40] C.R. McCormick, R.E. Schaak, *J. Am. Chem. Soc.* 143 (2021) 1017–1023.

[41] S. Hou, X. Ma, Y. Shu, J. Bao, Q. Zhang, M. Chen, P. Zhang, S. Dai, *Nat. Commun.* 12 (2021) 5917.

[42] L. Li, G. Chen, H. Zheng, W. Meng, S. Jia, L. Zhao, P. Zhao, Y. Zhang, S. Huang, T. Huang, J. Wang, *Nat. Commun.* 12 (2021) 3863.

[43] S. Selim, E. Pastor, M. García-Tecedor, M.R. Morris, L. Francàs, M. Sachs, B. Moss, S. Corby, C.A. Mesa, S. Gimenez, A. Kafizas, A.A. Bakulin, J.R. Durrant, *J. Am. Chem. Soc.* 141 (2019) 18791–18798.

[44] D.A. Muller, N. Nakagawa, A. Ohtomo, J.L. Grazul, H.Y. Hwang, *Nature* 430 (2004) 657–661.

[45] Y. Zheng, K. Fu, Z. Yu, Y. Su, R. Han, Q. Liu, *J. Mater. Chem. A* 10 (2022) 14171–14186.

[46] J.H. Lee, S. Lee, T. Kim, H. Ahn, G.Y. Jang, K.H. Kim, Y.J. Cho, K. Zhang, J.-S. Park, J.H. Park, *Joule* 7 (2023) 380–397.

[47] J. Zhu, F. Cannizzaro, L. Liu, H. Zhang, N. Kosinov, I.A.W. Filot, J. Rabeh, A. Brückner, E.J.M. Hensen, *ACS Catal.* 11 (2021) 11371–11384.

[48] Q. Zhang, K. Zhang, D. Xu, G. Yang, H. Huang, F. Nie, C. Liu, S. Yang, *Prog. Mater. Sci.* 60 (2014) 208–337.

[49] J. Rojas, E. Sun, G. Wan, J. Oh, R. Randall, V. Haribal, I.-h Jung, R. Gupta, A. Majumdar, *ACS Sustain. Chem. Eng.* 10 (2022) 12252–12261.

[50] X. Gao, L. Cao, Y. Chang, Z. Yuan, S. Zhang, S. Liu, M. Zhang, H. Fan, Z. Jiang, *ACS Sustain. Chem. Eng.* 11 (2023) 5597–5607.

[51] L. Yang, L. Pastor-Pérez, J.J. Villora-Pico, A. Sepúlveda-Escribano, F. Tian, M. Zhu, Y.-F. Han, T. Ramirez Reina, *ACS Sustain. Chem. Eng.* 9 (2021) 12155–12166.

[52] X. Zhang, X. Zhu, L. Lin, S. Yao, M. Zhang, X. Liu, X. Wang, Y.-W. Li, C. Shi, D. Ma, *ACS Catal.* 7 (2017) 912–918.

[53] X. Shi, H. He, L. Xie, *Chin. J. Catal.* 36 (2015) 649–656.

[54] R. Hu, S. Jin, G. Sha, *Prog. Mater. Sci.* 117 (2021) 100740.

[55] B. Wang, M. Wang, L. Han, Y. Hou, W. Bao, C. Zhang, G. Feng, L. Chang, Z. Huang, J. Wang, *ACS Catal.* 10 (2020) 9034–9045.

[56] X. Hu, J. Chen, W. Qu, R. Liu, D. Xu, Z. Ma, X. Tang, *Environ. Sci. Technol.* 55 (2021) 5435–5441.

[57] S. Li, L. Song, J. Li, H. He, *ACS Catal.* 13 (2023) 2867–2884.

[58] Y. Li, Y. Li, P. Wang, W. Hu, S. Zhang, Q. Shi, S. Zhan, *Chem. Eng. J.* 330 (2017) 213–222.

[59] Y. Lyu, J. Xu, Q. Cao, Z. Zhou, W. Hu, X. Liu, *J. Hazard. Mater.* 436 (2022) 129041.

[60] Y. Zhang, P. Glarborg, K. Johansen, M.P. Andersson, T.K. Torp, A.D. Jensen, J. M. Christensen, *ACS Catal.* 10 (2020) 1821–1827.